Sensitivity Study of Self-Piercing Rivet Insertion Process Using Smoothed Particle Galerkin Method

Li Huang[1], Youcai Wu[2], Garret Huff[1], Andrey Ilinich[1], Amanda Freis[1], Shiyao Huang[1], George Luckey[1]
[1]Ford Motor Company
[2]Livermore Software Technology Corporation

Abstract

Self-piercing rivets (SPR) are efficient and economical joining elements for automotive body structures manufacturing. The Smoothed Particle Galerkin Method has been initially proven as a potentially effective way to assess the SPR joining process. However, uncertain CAE parameters could result in significant mismatches between the CAE predictions and physical tests, and therefore the sensitivity study on critical model parameters is important to guide the modeling of the SPR insertion process. In this paper, a meshfree, i.e., Smoothed Particle Galerkin (SPG), method was applied to the simulation of the SPR insertion process with LS-DYNA®/explicit. The severely deformed upper sheet was modeled using the SPG method with activated bond failure, while the rest of the model was modeled using the traditional finite element approach. An extensive sensitivity study is conducted to understand the effect of a set of model parameters. This work provides a foundation for CAE model calibration for the SPR insertion process using SPG.

Keywords: Smoothed Particle Galerkin (SPG); self-piercing rivet

1. Introduction

The constant growth of designs and materials applied in a Body-in-White (BIW) are driving the complexity in the body joining processes. Traditional thermal joining techniques have some inherent challenges in dissimilar metal joining. Self-piercing rivets (SPR) are mechanical joining elements, and SPR joints are considered as one of the feasible joining approaches for lightweight materials such as aluminum and magnesium alloys, and composite materials. A SPR joint is produced by piercing a tubular or semi-tubular rivet into two or more substrate materials. The rivet manufactured from advanced high strength steel is pierced through the top sheets and expands in the bottom sheet to form mechanical interlock. The SPR insertion process can be divided into four steps: clamping, piercing, flaring, and releasing, as shown in Fig. 1. The traditional SPR joint development process is based on trial-and-error experiments and engineering experience. Such development may require many samples to test a variety of combinations, and a numerical simulation of the riveting process could significantly boost efficiency.

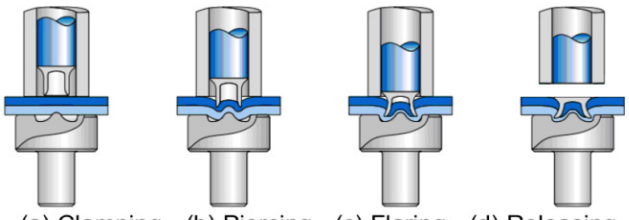

Fig. 1 Self-piercing rivet insertion process [1].

Various commercial software has been used for SPR insertion process simulation, including LS-DYNA, ABAQUS/Explicit, MSC.Simufact and DEFORM-2D etc. Most of the existing approaches implemented two-dimensional (2D) axisymmetric models [2-7] for simplicity, while full or partial 3D models [8-10] are still under development. To the best knowledge of the authors, in 1997, King et al [11] proposed the first finite element model for SPR process in DEFORM-2D. Till now, extensive research has been performed to improve the robustness and accuracy of SPR process modeling including material constitutive models, fracture criteria, interfacial friction profiles, contact settings, etc. [12, 13]. Despite the academic progress in the last two decades, a huge gap remains before CAE could efficiently guide the process optimization for SPR.

Two key issues for the SPR insertion process simulation are the extreme deformation and subsequent material failure during the piercing of substrates, which is not computationally stable or efficient with a traditional finite element method (FEM). The piercing step comes with material fracture, which can be modeled by geometrical or physical criteria. For the geometrical criterion, the upper layer minimum thickness, at which the sheet would separate, needs to be defined, which is hard to determine for general cases. The physical criteria are generally based on metrics derived from stress and strain tensors [4] or phenomenological damage [3].Usually, the fracture is implemented by element deletion, which can result in non-physical energy and volume loss. The re-meshing technique could reduce the element distortion, but at the same time it could introduce significant numerical errors during state and field variable mapping, resulting in inconsistent cross-section predictions in 2D mode [7], while 3D adaptive re-meshing is not numerically stable in current commercial solvers.

Meshfree methods do not require connections between nodes within the simulation domain; they construct approximation functions based on discrete nodes. Meshfree method offers unique advantages compared to the conventional FEM in the modeling of large material deformation, moving strong discontinuities, and immersed structures [14]. Meshfree approaches have been developed in the past several decades, and they have become increasingly applicable to simulate both fluid flow and solid mechanics applications. However, numerical instabilities, such as tension instability [15], spurious energy mode [16], and particle support related convergence [17], are encountered in the application of meshfree methods. Recently, Wu et. al [14, 18-20] developed the Smoothed Particle Galerkin (SPG) method using the direct nodal integration (DNI) technique. Detailed formulations of the SPG method can be found in literature [14, 19, 20]. To take the advantage of the SPG method, Huang and Wu et al [21] proposed a hybrid SPG-FEM 3D model for SPR insertion process, in which the most severely deformed region was modeled by SPG, a mesh free method, while the rest was FEM based. An agreement between the simulation and experiment has been initially achieved in terms of cross-sectional profile, but further improvement and sensitivity study is needed.

This paper presents a novel approach to reproduce SPR insertion process simulation using SPG method, and extensive sensitivity study is conducted to understand the effect of a set of model parameters. The rest of the paper is organized as follows: the material properties and basic experimental setup are given in Section 2; the CAE modeling strategy and virtual test matrix for sensitivity study is presented in Section 3; the simulation results are discussed in Section 4; and conclusions are made in Section 5.

2. Material Properties and Experiments

Two layers of 2.0 mm AA6111-T4 sheet were riveted by a Henrob servo-electric SPR gun. The rivet and die geometries are shown in Fig. 2(a) and Fig. 2(b), respectively. The final cross-section profile of the SPR joint is shown in Fig. 2(c). There are two key geometrical characteristics for evaluation of the quality of a SPR Joint, bottom layer thinning (BLT) and interlock (IL). BLT is defined as the thinnest part of the plastically deformed bottom layer material, and IL is defined as the distance between the rivet leg tip and the center-most captured point of the lower material in the joint. Table 1 summarizes the basic characteristic dimensions: rivet length L,

head diameter D_1, and shank diameter D_2, while the die has two key variables: die diameter D_0, and die depth H'.

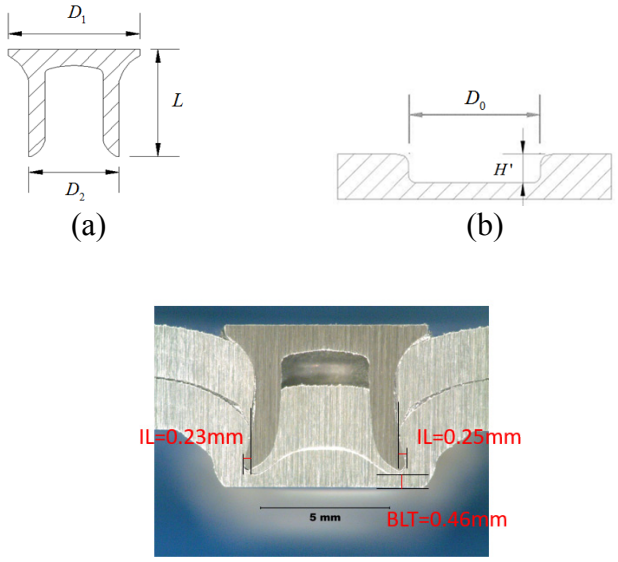

Fig. 2 Geometrical profiles of the (a) rivet and (b) die, and (c) the cross-section of a SPR joint (2 layers of 2.0mm AA6111-T4)

Basic material properties are listed in Table 2, where E is the young's modulus; $\sigma_{0.2}$ is the yield stress; E_t is the tangent modulus; K is the strength coefficient and n is the hardening exponent for the power law. The rivet material properties were obtained from lateral compression tests of rivet shank [4]. For simplicity, no temperature or strain rate effect was considered in this study.

Table 1 Geometrical profile of rivet and die

Top sheet (TS)	Bottom sheet (BS)	Rivet			Die	
T_1 (mm)	T_2 (mm)	D_1 (mm)	D_2 (mm)	L (mm)	D_0 (mm)	H' (mm)
2.0	2.0	7.8	5.3	6.5	10	2.2

Table 2 Material properties of rivet and workpieces

Material	E (Gpa)	$\sigma_{0.2}$ (Mpa)	E_t	K	n
AA 6111-T4	70	150	-	408	0.18
Rivet	210	1750	1650	-	-

3. Numerical Modeling

CAE analysis of rivet insertion process was performed using the commercial solver LS-DYNA®/explicit. A 3D hybrid SPG-FEM model [21] was proposed and only the most severely deformed region was modeled by SPG, while the rest of the model was FEM based. The center portion of TS where large deformation and material fracture occurs was modeled using SPG particles, while all the other remaining parts were modeled by FEM to

avoid excessive increase of computational cost. Critical parameters of the baseline model are given in Table 3. Averaged particle distance was about 0.2 mm, and the normalized nodal support size was set to 1.8 to define the influence domain of each particle. An updated Lagrangian kernel was adopted as the kernel approximation with updates performed every 20 explicit time steps. Based on previous researches [21], it is important to note that this proposed CAE approach did not show significant sensitivity to the main SPG parameters: bond failure criterion, kernel update frequency, kernel support size, particle distance, or mass scale.

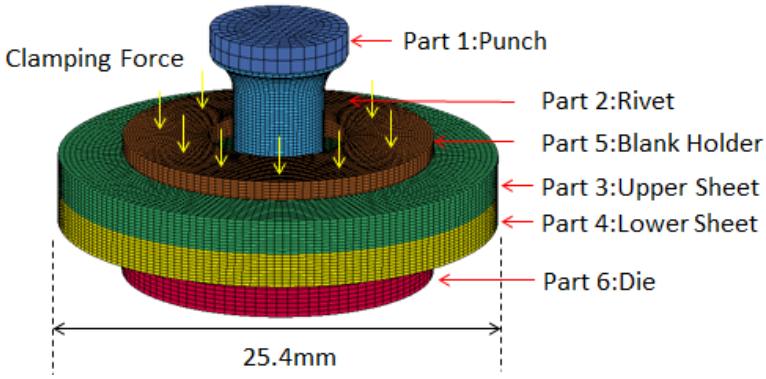

(a)

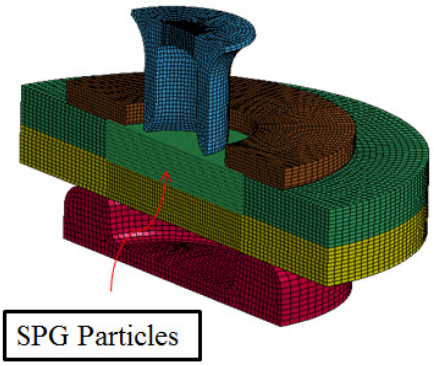

(b)

Fig. 3 Initial configuration of SPR process simulation (a) Overview of the 3D hybrid SPG-FEM model (b) Center portion of TS modeled by SPG.

Table 3 Summary of parameters for the baseline model

TS – the center portion	SPG, elastic-plastic with bond failure
TS– the outer portion	FEM, elastic-plastic
Rivet and BS	FEM, elastic-plastic
Punch, blank holder and die	FEM, rigid
Averaged SPG particle distance (mm)	0.2
Averaged FEM element size (deformable) (mm)	0.2
Punch Travel Distance (mm)	6.5
Coefficient of friction at interfaces	0.2
Blank holder Clamping force (kN)	7
SPG kernel update frequency	5
Mass scaling factor	2500

Proper boundary conditions were applied. The work pieces were clamped with constant normal force, and free boundary condition was applied at the outer edge. The punch travel velocity was set as constant for simplicity

and likely had minimal impact due to the rate insensitive material model. The simulation was terminated once the rivet head became nearly flush to TS surface. The coefficient of friction (COF) was fixed at 0.2 for both static and dynamic contacts at all interfaces. For fracture method, the bond-based failure criterion was applied for SPG parts. The critical effective plastic strain for bond failure was set at 0.54 based on the experimental data for AA6111-T4 [4], and has been explained and initially verified in previous researches [21].

To further understand the influence of physical parameters to the final configuration of the joint, a series of virtual tests were proposed, as given in Table 4. The test matrix was created with combinations of some selected critical physical parameters, including yield strength of rivet and workpieces, COF between parts involved, clamping force, sheet thickness and rivet length. The motivation of such sensitivity study is to get a preliminary insight into the impact of selected input variables, and the test matrix was not designed for a standard factorial analysis to avoid excessive requirements on CPU times and post-analysis. Case 1 is the baseline model. Note that reasonable maximum and minimum values were chosen, so that variations of selected parameters would potentially make a difference on the output but still could represent typical conditions in real engineering applications. The COF values were studied between paired contact parts involved, including: rivet and workpieces, blankholder and BS, Die and TS, and TS and BS. In order to keep the rivet head to be approximately flush for the final configuration of joint, the punch travel was adjusted accordingly for cases with sheet thickness and rivet length changes.

Table 4 Virtual Test Matrix for Sensitivity Study of Physical Parameters

Case No	Yield Stress Scale Factor		COF at Interfaces				Clamp Force (KN)	Sheet Thickness (mm)	Rivet Length (mm)
	Rivet	Workpieces	Rivet/ Workpieces	Holder/BS	Die/BS	TS/BS			
1*	1	1	0.2	0.2	0.2	0.2	7	2	6
2	0.8	1	0.2	0.2	0.2	0.2	7	2	6
3	1.2	1	0.2	0.2	0.2	0.2	7	2	6
4	1	0.8	0.2	0.2	0.2	0.2	7	2	6
5	1	1.2	0.2	0.2	0.2	0.2	7	2	6
6	1	1	0.02	0.2	0.2	0.2	7	2	6
7	1	1	0.3	0.2	0.2	0.2	7	2	6
8	1	1	0.2	0.02	0.2	0.2	7	2	6
9	1	1	0.2	0.3	0.2	0.2	7	2	6
10	1	1	0.2	0.2	0.02	0.2	7	2	6
11	1	1	0.2	0.2	0.3	0.2	7	2	6
12	1	1	0.2	0.2	0.2	0.02	7	2	6
13	1	1	0.2	0.2	0.2	0.3	7	2	6
14	1	1	0.2	0.2	0.2	0.2	4	2	6
15	1	1	0.2	0.2	0.2	0.2	10	2	6
16	1	1	0.2	0.2	0.2	0.2	7	1.9	6
17	1	1	0.2	0.2	0.2	0.2	7	2.1	6
18	1	1	0.2	0.2	0.2	0.2	7	2	5.9
19	1	1	0.2	0.2	0.2	0.2	7	2	6.1

* The baseline model

Six system responses were evaluated for the sensitivity study, including interlock (INT), bottom layer thinning (BLT), slug gap (SG), rivet final length (RFL), rivet tail flaring (RTF) and peak punch force (PPF). SG is the

central distance between the top and bottom surface of the slug within the rivet bore, RFL is the rivet length at the final configuration, RTF is the rivet flaring distance at the rivet tail, and PPF is the maximum punch force imposed during the riveting process. The geometrical responses are illustrated in Fig. 4. Only INT and BLT, which are the most important geometrical features, were used for the base model verification, and then additional four system responses were added for further sensitivity study.

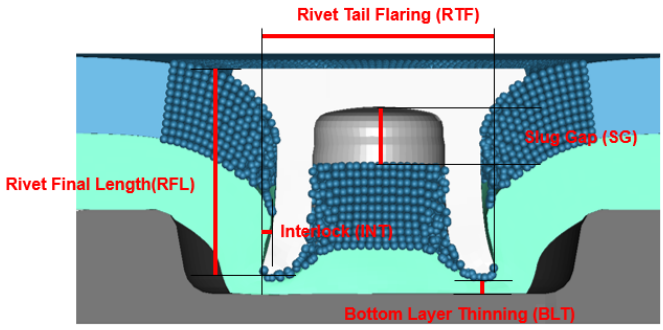

Fig. 4 Typical measurements on cross-sections

4. Result and Discussion

The cross-section profile predicted by the baseline model is compared to the experimental cross-section in Fig. 5. Typical measurements are listed in Table 5, and most important values are INT and BLT. From the cross-section comparison, the proposed model reasonably predicted the geometrical features, and the local deviation on the contour (RFL, RTF and SG) could be partially explained by an overly-stiff response of BS during penetration of rivet tail, which may be solved by reductions of element distortion through introduction of a similar meshfree approach for BS. Importantly, the large deformation and fracture during piercing were simulated successfully without any artificial stabilization, parameter tuning or element erosions.

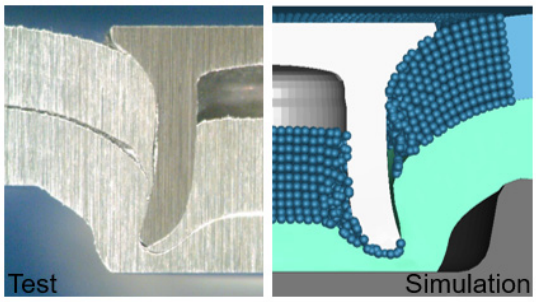

Fig. 5 Geometry comparisons between simulation and test (The baseline model)

Table 5 Comparisons between simulation and test on critical measurements (The baseline model) (unit: mm)

	INT	BLT	RFL	RTF	SG
Experimental Measurements	0.24	0.46	4.96	6.37	1.22
The baseline CAE model	0.28	0.43	5.49	6.16	1.52

Table 6 illustrates system responses from the sensitivity study for each case, including both geometrical and force output. As for geometrical output, the influence on the INT and BLT, which are two most important parameters in the quality evaluation of a SPR Joint, is further summarized in Fig. 6, which is based on the difference between CAE cases from the lower and upper factor boundary. Similarly, the influence on the SG, which is another important indicator for fine tuning of the CAE model, is also shown in Fig. 7. As for the punch force output, all results are illustrated in Fig. 8.

Table 6 System responses from the simulation for the sensitivity study

No	Cross-Section (mm)					PPF (KN)	Comments
	INT	BLT	RFL	RTF	SG		
1	0.28	0.43	5.49	6.16	1.52	38.8	The Baseline Model
2	0.24	0.38	5.55	6.07	1.50	37.2	Rivet Yield Strength Variation
3	0.32	0.53	5.38	6.39	1.55	39.0	
4	0.29	0.55	5.36	6.31	1.56	32.9	Work Piece Yield Strength Variation
5	0.22	0.30	5.63	6.00	1.50	43.3	
6	0.33	0.44	5.46	6.27	0.95	36.3	COF (Rivet/Workpieces) Variation
7	0.24	0.38	5.54	6.11	1.60	40.5	
8	0.29	0.40	5.52	6.17	1.51	38.7	COF (Holder/BS) Variation
9	0.29	0.44	5.48	6.17	1.52	39.0	
10	0.26	0.37	5.54	6.11	1.79	39.0	COF (Die/BS) Variation
11	0.30	0.44	5.47	6.20	1.46	38.9	
12	0.31	0.47	5.45	6.23	1.61	37.7	COF (TS/BS) Variation
13	0.25	0.43	5.49	6.12	1.49	38.2	
14	0.28	0.41	5.52	6.15	1.52	38.1	Clamping Force Variation
15	0.28	0.41	5.51	6.16	1.53	39.5	
16	0.27	0.43	5.49	6.18	1.67	31.2	Sheet Thickness Variation
17	0.29	0.46	5.46	6.17	1.37	44.4	
18	0.26	0.47	5.45	6.12	1.53	36.6	Rivet Length Variation
19	0.31	0.39	5.53	6.23	1.50	40.1	

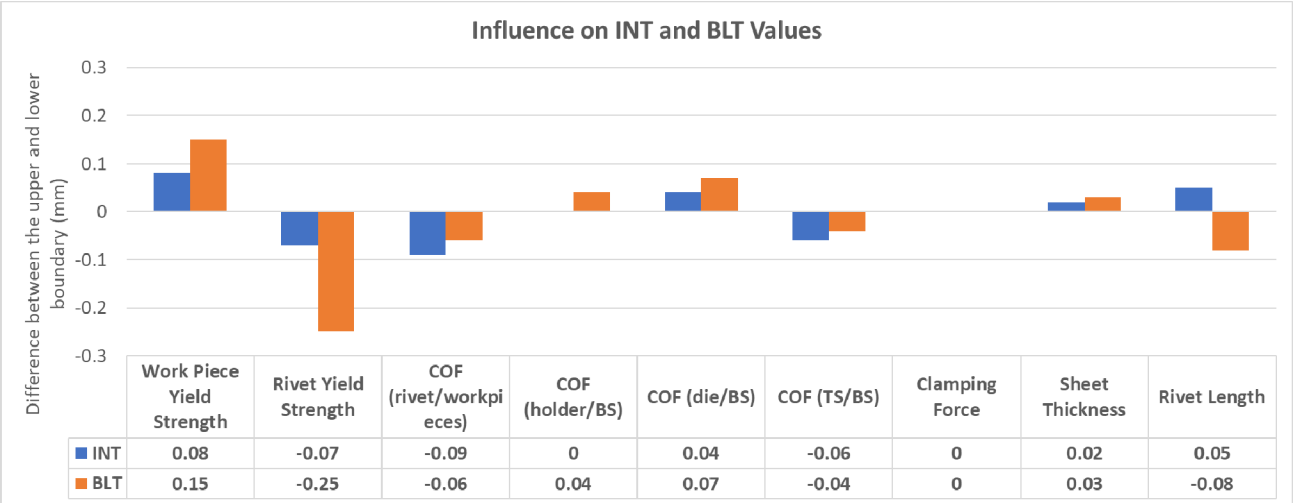

Fig. 6 Summary of influence on INT and BLT values

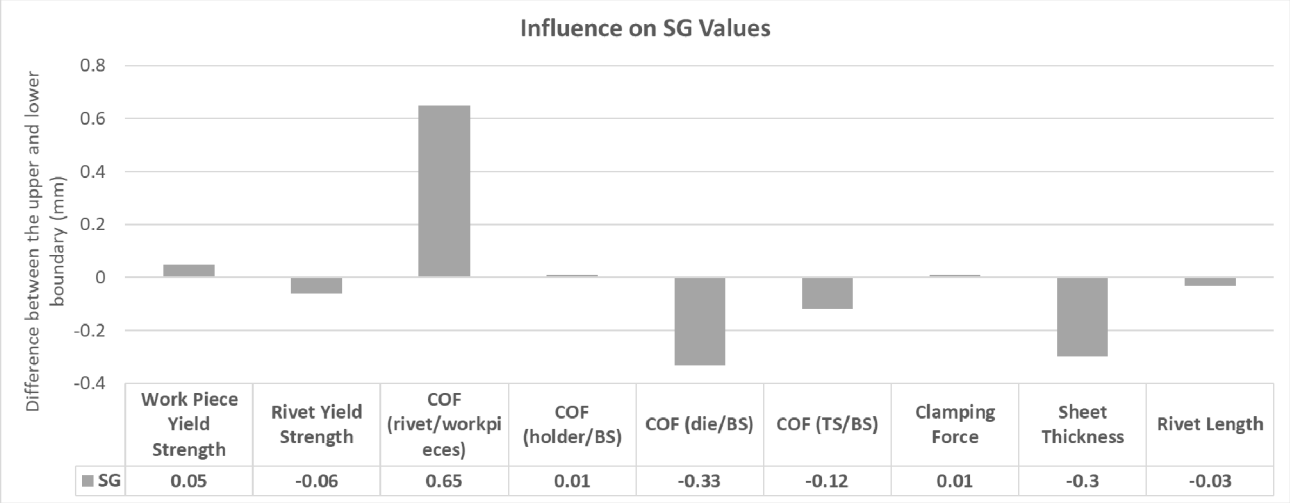

Fig. 7 Summary of influence on SG values

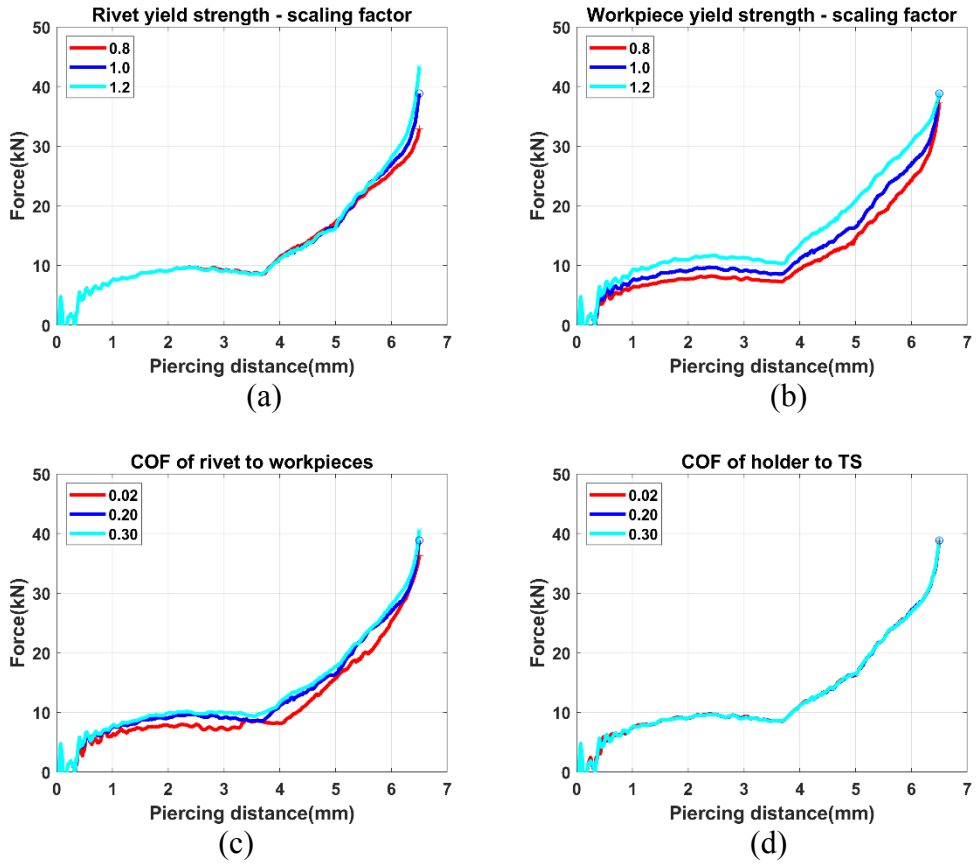

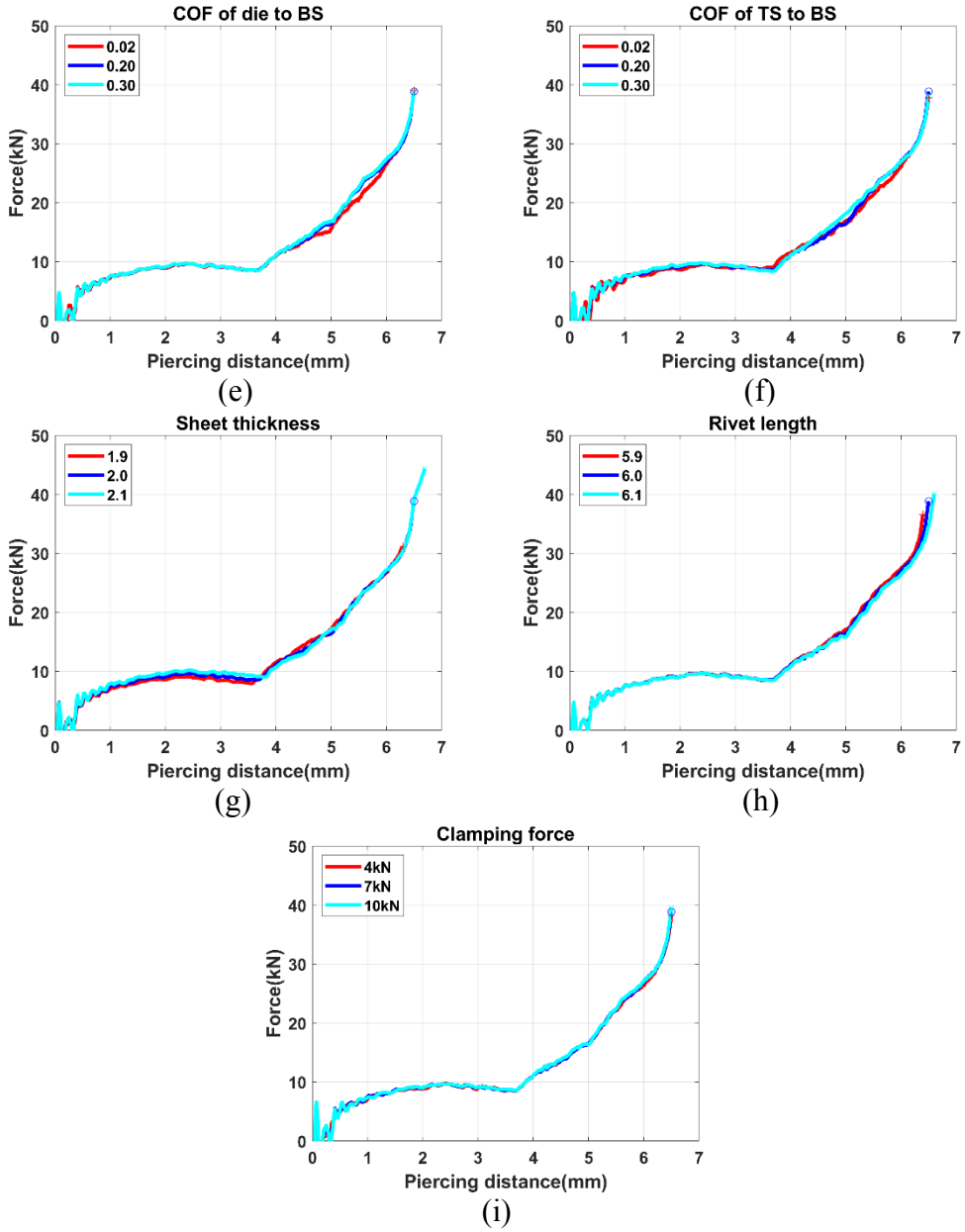

Fig. 8 Simulated force-displacement curves: (a) rivet yield strength, (b) workpiece yield strength m, (c) COF of rivet to workpieces, (d) COF of holder to TS, (e) COF of die to BS, (f) COF of TS to BS, (g) sheet thickness, (h) rivet length, (i) clamping force

From the geometrical responses, it could be seen that the most significant factors to INT and BLT is the yield strength of workpieces and rivet, while the most significant factors to SG is COF between rivet and work pieces. As the rivet yield strength increases, the rivet leg becomes harder to deform, resulting in less flaring and more penetration into the bottom layer. In this way, both INT and BLT tend to decrease. In the contrary, if the yield strength of work pieces increases, it becomes relatively harder for rivet to go through, resulting in less rivet flaring and more rivet normal compression. In this way, both INT and BLT tends to increase, although there are some exceptions in practice. The substrate material, AA6111-T4, is a precipitation hardening aluminum alloy, and it hardens over time stored at room temperature. Therefore, the consideration of its initial strength and natural aging effect can be used to accommodate the full material usage window. Similarly, joining process parameters may be not applicable to the substantially similar alloy from a material different supplier.

From the punch force responses, it could be noted that the top three significant factors are rivet yield strength, sheet thickness, and COF between rivet and work pieces. As the rivet becomes harder, it requires more energy to reach a flush joint. Similarly, as COF between rivet and work pieces increases, it becomes harder for rivet to penetrate substrate and also increases the resistance of material flow, which re-highlights the importance of lubricant on the rivet surface.

Overall, the sensitivity study highlighted the importance of obtaining accurate elastic-plastic properties, especially hardening for the joined materials and the rivet, and COF between rivet and work pieces should be set or calibrated based on real engineering conditions. At the same time, it should be noted that clamping force shows no significant impact to any outputs. However, all faying surfaces (materials and tooling) are in full contact with one another, both in physical tests and simulation. If additional force were required to close a gap, the force may contribute more to the joint quality metrics.

5. Summary

This paper describes a novel numerical methodology to reproduce the SPR insertion process using a hybrid SPG-FEM 3D model. A reasonable agreement between the simulation and experiment has been achieved in terms of cross-sectional profile with a baseline setting, and then an extensive sensitivity study is performed to understand the effect of a set of physical parameters, including yield strength of rivet and workpieces, COF between parts involved, clamping force, sheet thickness and rivet length.

From the sensitivity study, the clamping force does not significantly impact any output. For the cross-section profile, the simulation results show significance to the parameters: work piece yield strength, rivet yield strength and COF between rivet and work pieces. For the punch force profile, it is important to address attentions to rivet yield strength, sheet thickness, and friction between rivet and work pieces, which appear to have the biggest impact on the force response.

In summary, this work presents an attractive and robust way to reproduce joining processes by a meshfree method, and it provides an insight into critical model parameters through the sensitivity study. Since uncertain CAE parameters could result in significant mismatches between the CAE predictions and physical tests, this work also provides a foundation for further CAE model calibration of SPR insertion process using SPG.

Reference

[1] Self-pierce riveting for perfect joints, Boellhoff cooperation, (2010).
[2] B. Sui, C.B. Du D, H. Huang, L. Wang, Simulation and analysis of self-piercing riveting process in aluminum sheets, Mater Sci Technol, 15 (2007) 713-717.
[3] G. Casalino, A. Rotondo, A. Ludovico, On the numerical modelling of the multiphysics self piercing riveting process based on the finite element technique, Advances in Engineering Software, 39 (2008) 787-795.
[4] L. Huang, J.V. Lasecki, H. Guo, X. Su, Finite element modeling of dissimilar metal self-piercing riveting process, SAE International Journal of Materials and Manufacturing, 7 (2014) 698-705.
[5] L. Huang, J. Moraes, D.G. Sediako, J. Jordon, H. Guo, X. Su, Finite-Element and Residual Stress Analysis of Self-Pierce Riveting in Dissimilar Metal Sheets, Journal of Manufacturing Science and Engineering, 139 (2017) 021007.
[6] J.F.C. Moraes, J.B. Jordon, D.J. Bammann, Finite Element Analysis of Self-Pierce Riveting in Magnesium Alloys Sheets, Journal of Engineering Materials and Technology, 137 (2014) 021002.
[7] R. Porcaro, A.G. Hanssen, M. Langseth, A. Aalberg, Self-piercing riveting process: An experimental and numerical investigation, Journal of Materials Processing Technology, 171 (2006) 10-20.
[8] J.F.C. Moraes, H.M. Rao, J.B. Jordon, M.E. Barkey, High cycle fatigue mechanisms of aluminum self-piercing riveted joints, Fatigue & Fracture of Engineering Materials & Structures, 41 (2018) 57-70.
[9] J. Moraes, J. Jordon, E. Ilieva, Influence of the friction coefficient in self-pierce riveting simulations: a statistical analysis, SAE International Journal of Materials and Manufacturing, 11 (2018) 123-130.
[10] J. Moraes, J. Jordon, X. Su, M. Barkey, C. Jiang, E. Ilieva, Effect of process deformation history on mechanical performance of AM60B to AA6082 self-pierce riveted joints, Engineering Fracture Mechanics, 209 (2019) 92-104.

[11] R.P. King, J.M. O'Sullivan, D. Spurgeon, P. Bentley, Setting load requirements and fastening strength in the self-pierce riveting process, in: Proceedings of the 11th National Conference on Manufacturing Research, 1995, pp. 57-61.
[12] D. Li, A. Chrysanthou, I. Patel, G. Williams, Self-piercing riveting-a review, The International Journal of Advanced Manufacturing Technology, 92 (2017) 1777-1824.
[13] X. He, F. Gu, A. Ball, Recent development in finite element analysis of self-piercing riveted joints, The international journal of advanced manufacturing technology, 58 (2012) 643-649.
[14] C.T. Wu, T.Q. Bui, Y. Wu, T.-L. Luo, M. Wang, C.-C. Liao, P.-Y. Chen, Y.-S. Lai, Numerical and experimental validation of a particle Galerkin method for metal grinding simulation, Computational Mechanics, (2017).
[15] J. Swegle, D. Hicks, S. Attaway, Smoothed particle hydrodynamics stability analysis, Journal of computational physics, 116 (1995) 123-134.
[16] S. Beissel, T. Belytschko, Nodal integration of the element-free Galerkin method, Computer methods in applied mechanics and engineering, 139 (1996) 49-74.
[17] T. Belytschko, Y. Krongauz, J. Dolbow, C. Gerlach, On the completeness of meshfree particle methods, International Journal for Numerical Methods in Engineering, 43 (1998) 785-819.
[18] C.T. Wu, M. Koishi, W. Hu, A displacement smoothing induced strain gradient stabilization for the meshfree Galerkin nodal integration method, Computational Mechanics, 56 (2015) 19-37.
[19] C.T. Wu, Y. Wu, J.E. Crawford, J.M. Magallanes, Three-dimensional concrete impact and penetration simulations using the smoothed particle Galerkin method, International Journal of Impact Engineering, 106 (2017) 1-17.
[20] C.T. Wu, S.W. Chi, M. Koishi, Y. Wu, Strain gradient stabilization with dual stress points for the meshfree nodal integration method in inelastic analyses, International Journal for Numerical Methods in Engineering, 107 (2016) 3-30.
[21] L. Huang, Y. Wu, G. Huff, S. Huang, A. Ilinich, A. Freis, G. Luckey, Simulation of Self-Piercing Rivet Insertion Using Smoothed Particle Galerkin Method, (2018).